

Article

Heterostructured ZnCdS@ZIF-67 as a Photocatalyst for Fluorescent Dye Degradation and Selectively Nonenzymatic Sensing of Dopamine

Zhichao Wang ¹, Bianying Wen ^{2,*}, Jie Zhou ³, Xin Zhao ³, Xiaoyuan Zhang ^{3,*} and Zhiqiang Su ^{3,*} ¹ Precision Forestry Key Laboratory of Beijing, Beijing Forestry University, Beijing 100083, China² Key Laboratory of Processing and Quality Evaluation Technology of Green Plastics of China National Light Industry Council, Beijing Technology and Business University, Beijing 100048, China³ State Key Laboratory of Chemical Resource Engineering, Beijing Key Laboratory of Advanced Functional Polymer Composites, Beijing University of Chemical Technology, Beijing 100029, China

* Correspondence: weibianying@tsinghua.org.cn (B.W.); 2020700036@buct.edu.cn (X.Z.); suzq@mail.buct.edu.cn (Z.S.)

Abstract: Dopamine (DA) plays the role of the transmitter of information in the brain. Neurological diseases and depression are in close relationship with DA release. In this study, we developed a co-catalyst Zn_{0.2}Cd_{0.8}S@zeolitic imidazolate framework-67 (Zn_{0.2}Cd_{0.8}S@ZIF-67) to improve the photocatalyst efficacy of Rhodamine B (RhB) and electrochemical sensing of DA. Results show that Zn_{0.2}Cd_{0.8}S@ZIF-67 exhibits optimal photocatalytic activity with the addition of 80 mg ZIF-67. The degradation percentage of RhB by Zn_{0.2}Cd_{0.8}S@ZIF-67 reached 98.40% when the co-catalyst was 50 mg. Radical trapping experiments show that ·O₂⁻ played a significant role in the photocatalytic degradation of RhB. The catalytic mechanism of the Zn_{0.2}Cd_{0.8}S@ZIF-67 was found as a Z-type photocatalysis. Finally, a DA biosensor was constructed and displayed a high response and selectivity to DA. This can be attributed to the heterojunction between Zn_{0.2}Cd_{0.8}S and ZIF-67, which can significantly enhance the separation of e⁻/h⁺ and improve charge transfer. These findings will play a positive role in the in-situ monitoring of neurological diseases and depression.

Keywords: photocatalytic degradation; ZnCdS; ZIF-67; Rhodamine B; dopamine sensor



Citation: Wang, Z.; Wen, B.; Zhou, J.; Zhao, X.; Zhang, X.; Su, Z.

Heterostructured ZnCdS@ZIF-67 as a Photocatalyst for Fluorescent Dye Degradation and Selectively Nonenzymatic Sensing of Dopamine. *Materials* **2022**, *15*, 7683. <https://doi.org/10.3390/ma15217683>

Academic Editor: Barbara Pawelec

Received: 22 September 2022

Accepted: 28 October 2022

Published: 1 November 2022

Publisher's Note: MDPI stays neutral with regard to jurisdictional claims in published maps and institutional affiliations.



Copyright: © 2022 by the authors. Licensee MDPI, Basel, Switzerland. This article is an open access article distributed under the terms and conditions of the Creative Commons Attribution (CC BY) license (<https://creativecommons.org/licenses/by/4.0/>).

1. Introduction

Dopamine (DA) is the most abundant catecholamine neurotransmitter in the brain. It plays an important role in the central nervous system, kidneys, cardiovascular system, and endocrine system [1]. DA levels can affect heart rate, leading to heart failure and Parkinson's disease [2]. Therefore, in situ measurement of DA content can be obtained using biosensors. Among them, electrochemical monitoring of DA is an excellent strategy [3]. Lee et al. [2] designed a ruthenium nanoparticle-immobilized multiscale pore-containing carbon nanofiber-based field-effect transistor nonenzymatic sensor to detect DA. They found that the porous carbon structure not only promoted the generation of small-size Ru particles, but also induced a large active surface area for DA. Dashtian et al. [4] formed heterojunction by coupling dendrite-like CuInSe₂(CIS) with Cu₂O nanoparticles. This PEC sensing system targeted DA within two working ranges from 0.1–5.5 μM and 5.5–150 μM at a low detection limit of 2.1 nM. Cu₂O/CIS acted as photoelectric converters and amplifier layers for PEC-sensing. The signal quenching was obtained in the presence of DA due to a hindrance effect.

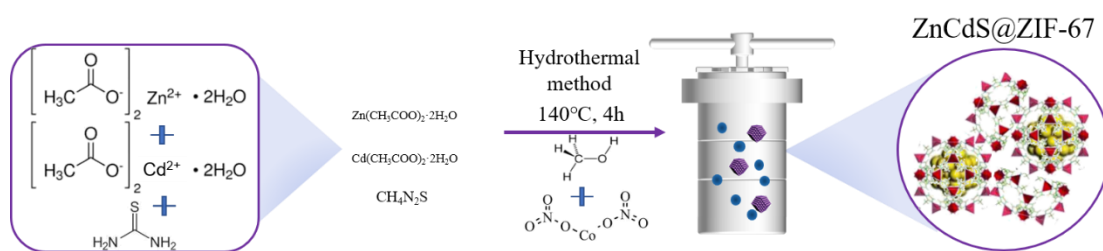
Metal ions and organic ligands can form metal-organic framework (MOF) materials with unique porous structures and large surface areas [5]. Due to the diversity of MOFs, the photoadsorption properties can be controlled by constructing organic ligands and metal ions [6–8]. Most metal nodes, such as Zr-O, Ti-O, and Cu-O clusters, do not have

a visible light response. Therefore, metals responsive to visible light can be substituted or doped to provide MOF with an excellent light trapping ability in the visible region. On the one hand, the energy band structure of MOFs needs to be fine-tuned to meet the reduction potential of the reaction. On the other hand, most MOFs are microporous, which allows the selectivity and limited reactivity to be regulated by the diffusion of the catalyst. Multi-stage porous MOFs can reduce the mass transfer resistance and hopefully allow for the conversion of larger reactants. Ngoc Tran et al. [9] fabricated gold nanoparticles/metal-organic frameworks (Au NPs/IRMOF-3) hybrids. Au NPs/IRMOF-3 multilayers generated chemical and electromagnetic amplification of Raman signals of RhB at a low concentration and high enhancement factor. This hybrid can be used for DA sensing with high sensitivity and stability (limit of detection is 1.42×10^{-18} M with a wide linear range from 10^{-17} to 6×10^{-8} M of DA).

Developing efficient photocatalytic systems depends mainly on designing and fabricating appropriate material combinations. They are usually combined with other semiconductors and metallic materials to reduce the agglomeration of different materials for efficient electron transfer [10]. Zhang et al. [11] prepared the Ag/Uio-66-NH₂ by soaking AgNO₃ into zirconium 1,4-dicarboxybenzene MOF (UiO-66) and then reducing it by NaBH₄. The photodegradation of Rhodamine B (RhB) dye by Ag/Uio-66-NH₂ under ultraviolet and visible light was better than that of the original UiO-66-NH₂. The built-in heterostructure accelerates electron-hole separation and absorption of visible light. Zeolitic imidazolate frameworks (ZIFs) molecular sieve comprises Zn²⁺, Co²⁺, and imidazole ligands. ZIF-67 is composed of metal ions Co²⁺ and 2-Methylimidazole. The broad surface area of ZIF-67 exposes more active sites in the photocatalysis process. Dong et al. [12] designed a WO₃/CsPbBr₃/ZIF-67 ternary heterostructure for efficient CO₂ photoreduction. The surface modification of zeolites with active Co sites in ZIF-67 promoted the adsorption and activation of CO₂. The synergistic effect of charge separation and CO₂ absorption greatly enhanced the photocatalytic activity. Kumar et al. [13] prepared a graphite nitride Ag@ZIF-67 complex and investigated its degradation of Methylene blue and Congo red (CR) dyes.

CdS has been regarded as a unique photocatalyst among II–VI compound semiconductors. The photodegradation efficacy of CdS is based on the dopant elements [14], such as Fe, Co, and Ni. Cd-S linkage, along with other functional groups in the spherical nanoparticles of Fe-CdS, was demonstrated [15]. The Fe-doped CdS NPs showed superior catalytic potential compared to undoped CdS. Zn_xCd_{1-x}S is a ternary photocatalyst with a controllable band gap and band edge position. It is necessary to find strategies to compensate for the deficiencies of ZnCdS and produce a better photocatalytic performance. Nanomaterials are combined with ZnCdS and reduce the occurrence of electron-hole pair recombination to a certain extent. Zhang et al. [16] synthesized MOF-derived porous hollow carbon nanobubbles@ZnCdS multi-shelled dodecahedral cages (C@ZnCdS MSDCs). C@ZnCdS MSDCs displayed superior photoelectrochemical (PEC) performance. The photoexcited electrons were transferred from the conduction band (CB) of C@ZnCdS MSDCs to the CB of TiO₂. Simultaneously, holes were transferred from the valence band (VB) of TiO₂ to the VB of C@ZnCdS MSDCs, leading to a boost of visible-light response and separation of photogenerated e⁻/h⁺.

In this study, we designed a Zn_{0.2}Cd_{0.8}S@ZIF-67 co-catalyst to form a heterojunction via a one-pot hydrothermal method (Scheme 1). Zn_{0.2}Cd_{0.8}S has excellent photocatalytic performance [17–20]. ZIF-67 promoted the exposure of active sites in catalytic reactions and the effect of Co on electrical conductivity. The combination of ZnCdS and ZIF-67 is supposed to play a synergistic effect in strengthening photocatalytic performance. In addition, the photocatalytic activity of Zn_{0.2}Cd_{0.8}S@ZIF-67 was evaluated by degrading the RhB solution and functioning as a DA sensor. Free radical trapping experiments were carried out to investigate the active substances, which play a significant role in the determination of selective sensing of DA.



Scheme 1. Schematic drawing of $\text{Zn}_{0.2}\text{Cd}_{0.8}\text{S@ZIF-67}$ via one-pot hydrothermal method.

2. Materials and Methods

2.1. Materials

The materials and reagents are as follows: 2-Methylimidazole (99%, J&K, Beijing, China), thiourea (99%, J&K, Beijing, China), potassium bromide (99%, J&K, Beijing, China), zinc dihydrate acetate (99%, J&K, Beijing, China), sodium sulfate (99%, J&K, Beijing, China), disodium ethylenediaminetetraacetic acid (EDTA) (99%, J&K, Beijing, China), benzoquinone (99%, J&K, Beijing, China), methanol ($\geq 99.7\%$, J&K, Beijing, China), isopropanol (99.5%, J&K, Beijing, China), Rhodamine B (96%, J&K, Beijing, China), anhydrous ethanol ($\geq 99.7\%$, Fuyu chemical, Tianjin, China), cobalt nitrate hexahydrate (98%, Damao chemical reagent factory, Tianjin, China), and cadmium acetate dihydrate (99%, Thermo Fisher Scientific, Waltham, MA, USA). The ITO slides are purchased from Luoyang Guluo Glas Co., Ltd. (Luoyang, China).

2.2. Synthesis of ZIF-67

Solution A was prepared by dissolving 1.45 g cobalt nitrate hexahydrate in 50 mL of methanol by agitation. We dissolved 3.2 g 2-Methylimidazole in 50 mL of methanol to form solution B. Solutions A and B were stirred for 24 h, then centrifuged with a low-speed centrifuge, and washed with ethanol and ultra-pure water. The purple precipitates were dried for 12 h in an oven at 60 °C. The product was ground into powder for subsequent use.

2.3. Synthesis of $\text{Zn}_{0.2}\text{Cd}_{0.8}\text{S@ZIF-67}$

$\text{Zn}_{0.2}\text{Cd}_{0.8}\text{S@ZIF-67}$ was prepared using the one-pot method. Specifically, 0.22 g of zinc dihydrate, 1.07 g of cadmium dihydrate, 0.38 g of thiourea, and different amounts (10, 30, 50, 70 mg) of ZIF-67 were dissolved in 80 mL of water. The mixed solution was ultrasonically treated for about 30 min and magnetically stirred for 30 min. The solution was then transferred to the lining of the Teflon autoclave, and treated at 140 °C for about 4 h. After the reaction was completed, the reactor was slowly cooled to room temperature. The product was then centrifuged, washed with water and ethanol, and dried for 12 h in an oven at 60 °C. The product was ground into powder for subsequent use.

2.4. Material Characterization

Information about the microscopic topography of the photocatalyst was obtained from the scanning electron microscope (SEM) images by using a Hitachi SU8010 SEM. The microstructure was characterized by the FEI-TALOS-F200X transmission electron microscope (TEM). From the Fourier transform infrared spectrometer (FTIR-650), information about the functional groups carried by the catalyst were obtained. The test wavelength range is set from 4000 to 400 cm^{-1} . An Ultima IV X-ray diffractometer (XRD) was used to analyze the structure of the samples. The element properties were studied by Thermo Scientific K-alpha+X-ray photoelectron spectroscopy (XPS). PerkinElmer and LAMADA950 ultraviolet-visible spectroscopy (UV-vis) provided UV absorption spectra and UV diffuse reflectance spectra. The ultraviolet diffuse reflectance spectroscopy (UV-vis DRS) displayed information about the light absorption by photocatalysts. Steady-state, transient fluorescence spectra of samples were obtained with a Hitachi F-4600 photometer. The Mott-Schottky curve, photocurrent

response, and Electrochemical Impedance Spectroscopy (EIS) Nyquist plot were measured on an electrochemical workstation (CHI760E).

2.5. Photocatalytic Degradation Experiment

The experimental procedure was as follows: 5 mg of RhB powder was dissolved in 500 mL ultra-pure water, 10 mg/L of RhB solution was obtained, and each photocatalytic reactor was filled with 50 mL of RhB solution. A total of 30 mg of photocatalyst was dispersed in the RhB solution with a magnetic stirrer in a 100 mL beaker. The catalyst sample was stirred at a constant speed for half an hour without light to reach an equilibrium point between the dye and the catalyst. With a 500 W Xe lamp, the 50 mL of dye solution was centrifuged every 30 min. After centrifugation, the RhB solution was tested for instant absorbance. The photocatalytic degradation efficiency (C/C_0) of RhB required its absorbance to be converted.

2.6. Free Radical Trapping Experiment

The RhB degradation by catalyst was characterized by a free radical trapping experiment. Ethylenediaminetetraacetic acid disodium (EDTA-2Na) was used as a trapping agent for h^+ , while benzoquinone (BQ) was used for benzoquinone ($\cdot O_2^-$) and isopropanol (IPA) was used for hydroxyl radicals ($\cdot OH$). A total of 30 mg of photocatalyst was dispersed in 50 mL of RhB solution with a 10 mg/L concentration. Then, the 50 mL of trapping agent was added to the degradation container, and the samples were stirred at a constant speed for half an hour in the dark to mix RhB and the catalyst before the actual illumination.

2.7. Fabrication of the DA Sensor

The fabrication of the photoelectrochemical (PEC) sensor was as follows: Indium Tin Oxide (ITO) electrodes were sonicated in acetone, absolute ethanol, and double distilled water for 10 min and then dried at room temperature. The 6 mg of $Zn_{0.2}Cd_{0.8}S@ZIF-67$ was then dispersed in a mixed solution of 45 μL ethanol and 5 μL 0.1% (w/w) Nafion, which was sonicated for 20 min. Then, 15 μL suspension droplets were drop-casted on the 1 cm \times 1 cm square centimeter ITO surface and dried at room temperature to obtain the ITO/ $Zn_{0.2}Cd_{0.8}S@ZIF-67$ electrode. The modified ITO electrode was used as the working electrode, the platinum plate electrode was used as the paired electrode, and the Ag/AgCl (saturated KCl solution) was used as a reference electrode. With the 500 W Xe lamp, the photoelectrochemical responses of the modified electrode to DA in 0.1 M phosphate buffered saline (PBS) solution were evaluated by chronoamperometry.

For the DA selectivity test, we selected Fructose, Lactic acid (LA), ascorbic acid (AA), sulfuric acid (UA), sucrose, glucose, and lactose as the interfering molecules for amperometric detection of DA using the CHI760E platform. These molecules co-exist in human blood plasma. The concentration of DA was 100 μM in 0.1 M PBS. The additional amount of interfering molecules was 100 μM in 0.1 M PBS.

3. Results and Discussion

3.1. Morphological and Structural Characterizations of $Zn_{0.2}Cd_{0.8}S@ZIF-67$

The SEM images can provide information about the microstructure of ZIF-67, $Zn_{0.2}Cd_{0.8}S$, $Zn_{0.2}Cd_{0.8}S@ZIF-67$. It can be seen from Figure 1a that $Zn_{0.2}Cd_{0.8}S$ has flower-like morphology, but with obvious agglomeration. Figure 1b shows the rhombic dodecahedron structure of ZIF-67, which has a smooth surface and large area. In Figure 1c,d, when ZIF-67 is doped in $Zn_{0.2}Cd_{0.8}S$, the surface morphology changes. $Zn_{0.2}Cd_{0.8}S@ZIF-67$ becomes coarser, and $Zn_{0.2}Cd_{0.8}S$ increases the surface area. The EDS diagram shows the C, O, S, Cd, Zn, and Co traces (Figure 1e).

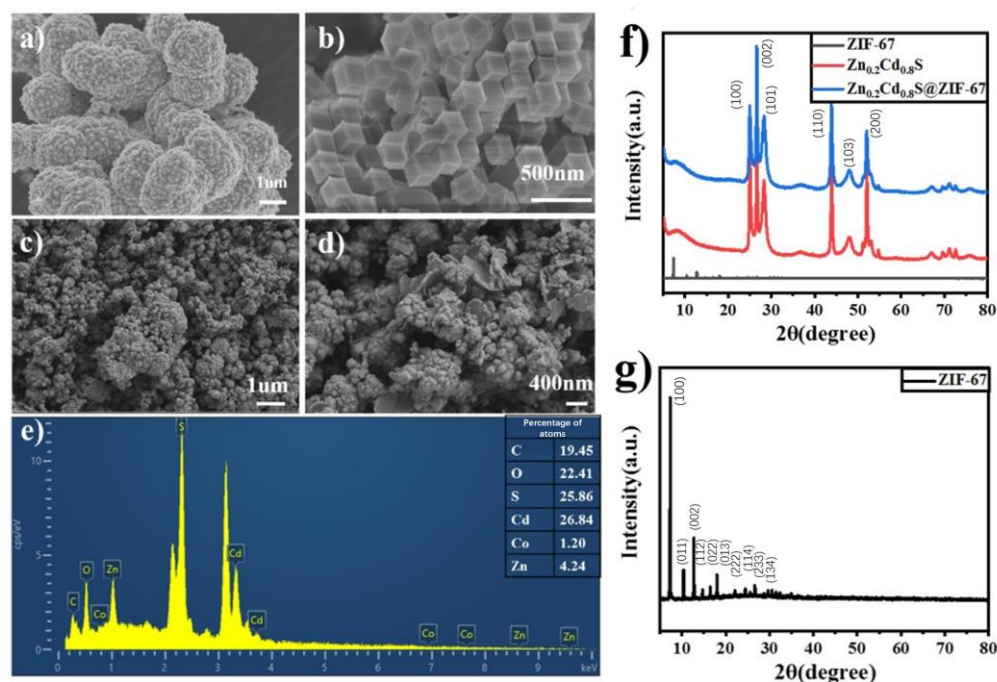


Figure 1. (a) SEM image of Zn_{0.2}Cd_{0.8}S; (b) ZIF-67; (c,d) Zn_{0.2}Cd_{0.8}S@ZIF-67; (e) EDX pattern of Zn_{0.2}Cd_{0.8}S@ZIF-67; XRD patterns of Zn_{0.2}Cd_{0.8}S (f) and Zn_{0.2}Cd_{0.8}S@ZIF-67 (g).

The diffraction patterns of Zn_{0.2}Cd_{0.8}S are at 25.19°, 26.62°, 28.16°, 43.56°, 47.99°, and 51.95° (JCPDS no. 49-1302), corresponding to (100), (002), (101), (110), (103), and (200) planes (Figure 1f). The peaks of Zn_{0.2}Cd_{0.8}S are sharp, indicating high crystallinity. The diffraction peaks of Zn_{0.2}Cd_{0.8}S are slightly weaker than those of Zn_{0.2}Cd_{0.8}S@ZIF-67, indicating a slightly positive effect of ZIF-67 on the Zn_{0.2}Cd_{0.8}S crystallization. The crystalline size and % crystallinity of Zn_{0.2}Cd_{0.8}S and Zn_{0.2}Cd_{0.8}S@ZIF-67 are shown in Table S1. From Figure 1g, the XRD patterns of ZIF-67 show obvious diffraction peaks at 7.46°, 10.47°, 12.52°, 14.76°, 16.50°, 22.40°, 24.56°, and 26.94°, corresponding to (011), (002), (112), (022), (013), (222), (114), (233), and (134) crystal faces, respectively. Since the content of ZIF-67 is small, the corresponding information of the EDS diagram Zn_{0.2}Cd_{0.8}S@ZIF-67 is weak in Figure 1e. Meanwhile, the diffraction peak intensity of ZIF-67 itself is significantly weaker than that of Zn_{0.2}Cd_{0.8}S and Zn_{0.2}Cd_{0.8}S@ZIF-67. Therefore, the peak value of ZIF-67 may also be submerged. The co-catalyst does not reflect the diffraction peak of ZIF-67.

Element analysis of Zn_{0.2}Cd_{0.8}S@ZIF-67 was performed using XPS (Figure 2a), in which the distribution of the Co element is very weak compared with the full spectrum of pure Zn_{0.2}Cd_{0.8}S. The distribution strength of Zn is increased, which may be due to the addition of ZIF-67, increasing the content of Zn in the total proportion. Two peaks of 404.5 eV and 411.2 eV in the XPS spectra of Cd 3d, corresponding to Cd 3d_{5/2}, Cd 3d_{3/2} (Figure 2b), were observed in contrast to the fine spectra of Cd 3d XPS in Figure S1. The binding energies of Cd 3d_{5/2} and Cd 3d_{3/2} in the catalyst decreased by 0.1 eV and 0.2 eV, respectively. The peak at 161.2 eV in the S 2p XPS map in Figure 2c belongs to S 2p_{3/2}, and the peak at S 2p_{1/2} corresponds to the peak at 162.4 eV. Compared with the fine spectrum of S 2p XPS, the binding energy at S 2p_{3/2} and S 2p_{1/2} increased by 0.1 eV and 0.2 eV, respectively. Figure 2d shows the high-resolution Zn 2p spectra resolved into peaks centered at 1021.4 eV and 1044.4 eV, corresponding to Zn 2p_{3/2} and Zn 2p_{1/2}. Compared to the fine spectra of Zn 2p XPS, the peak of Zn_{0.2}Cd_{0.8}S@ZIF-67 decreased by 0.1 eV. The change of Zn_{0.2}Cd_{0.8}S@ZIF-67 XPS binding energy may be due to crystalline size and electron concentrations. The electron concentrations are caused by the interface interaction and electron transfer in the heterojunction formed by two semiconductors. It is concluded that ZIF-67 and Zn_{0.2}Cd_{0.8}S interact with each other. Electron transfer exists between the two photocatalytic semiconductors, which proves that ZIF-67 was successfully

complexed with $\text{Zn}_{0.2}\text{Cd}_{0.8}\text{S}$. Co 2p can be decomposed into two distinct characteristic peaks: Co $2p_{3/2}$ corresponds to the binding energy of 781.1 eV, and Co $2p_{1/2}$ corresponds to the binding energy of 796.2 eV.

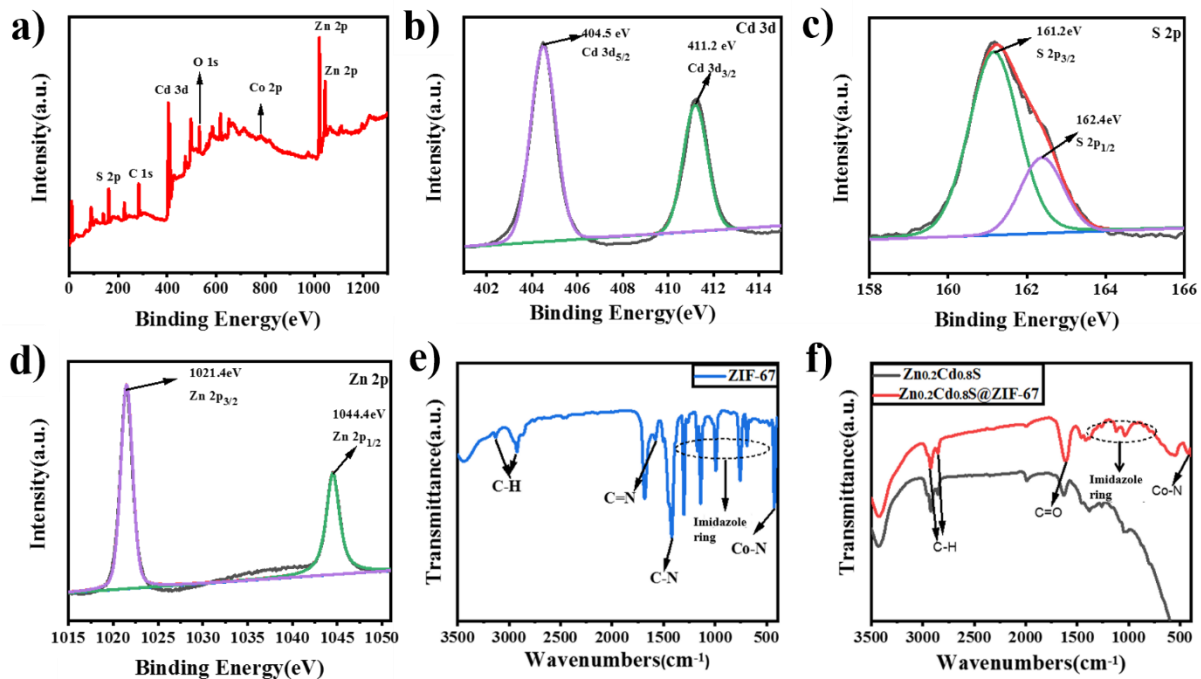


Figure 2. (a) Full scan XPS spectrum of $\text{Zn}_{0.2}\text{Cd}_{0.8}\text{S}@ \text{ZIF-67}$; (b) High-resolution XPS Cd 3d; (c) Zn 2p; (d) S 2p spectrum of $\text{Zn}_{0.2}\text{Cd}_{0.8}\text{S}@ \text{ZIF-67}$; FTIR spectra of (e) ZIF-67 and (f) $\text{Zn}_{0.2}\text{Cd}_{0.8}\text{S}@ \text{ZIF-67}$.

As can be seen in Figure 2e, the characteristic peaks at 3137 cm^{-1} and 2925 cm^{-1} correspond to the stretching vibration of C-H of aromatic hydrocarbon and aliphatic hydrocarbon in raw 2-Methylimidazole, respectively. The characteristic peak at 1419 cm^{-1} indicates the stretching vibration of C-N. The stretching vibration of C=N corresponds to the wavenumber 1573 cm^{-1} . The wavenumber of 424 cm^{-1} is the characteristic absorption peak belonging to Co-N. The out-of-plane vibration of the imidazole ring is shown by the characteristic peaks at wavenumbers of 1301 cm^{-1} , 1139 cm^{-1} , 993 cm^{-1} , 752 cm^{-1} , and 688 cm^{-1} . The results above indicate that ZIF-67 was synthesized successfully. The characteristic peaks of 3440 cm^{-1} correspond to the stretching peaks of O-H, while the stretching peaks of 2950 cm^{-1} and 2856 cm^{-1} represent the stretching peaks of C-H (Figure 2f). The wavenumbers of 1623 cm^{-1} and 1378 cm^{-1} are attributed to the stretching vibration of C=O and the stretching vibration of C-OH, respectively. These come from cadmium acetate and zinc acetate. Based on the infrared spectra of $\text{Zn}_{0.2}\text{Cd}_{0.8}\text{S}$, the strength of the $\text{Zn}_{0.2}\text{Cd}_{0.8}\text{S}@ \text{ZIF-67}$ at 1606 cm^{-1} C=O tensile vibration peak was obviously increased. The characteristic peak at 1120 cm^{-1} is evident, which corresponds to the plane vibration of the imidazole ring. A characteristic peak appears at about 570 cm^{-1} . At the same time, the characteristic peak of Co-N at 418 cm^{-1} is also observed. The above results show that ZIF-67 was successfully compounded on $\text{Zn}_{0.2}\text{Cd}_{0.8}\text{S}$.

3.2. Photoelectrochemical Performances and Analysis

Both $\text{Zn}_{0.2}\text{Cd}_{0.8}\text{S}$ and $\text{Zn}_{0.2}\text{Cd}_{0.8}\text{S}@ \text{ZIF-67}$ have absorption in the 200–500 nm wavelength. ZIF-67 has apparent UV absorption at 243 nm and 581 nm, as shown in Figure 3a. The bandgap of ZIF-67 is 1.94 eV (Figure 3b), and the bandgap of $\text{Zn}_{0.2}\text{Cd}_{0.8}\text{S}$ is 2.18 eV (Figure 3c). The bandgap of $\text{Zn}_{0.2}\text{Cd}_{0.8}\text{S}@ \text{ZIF-67}$ is 2.20 eV (Figure 3d), only increased to 0.2 eV. It can be seen that ZIF-67 can improve the light absorption capacity of $\text{Zn}_{0.2}\text{Cd}_{0.8}\text{S}$, but has little effect on the band gap. This is due to strong interaction and coupling effects of

$\text{Zn}_{0.2}\text{Cd}_{0.8}\text{S}$ and ZIF-67 at the interface. These effects decrease the recombination probability of electrons and holes.

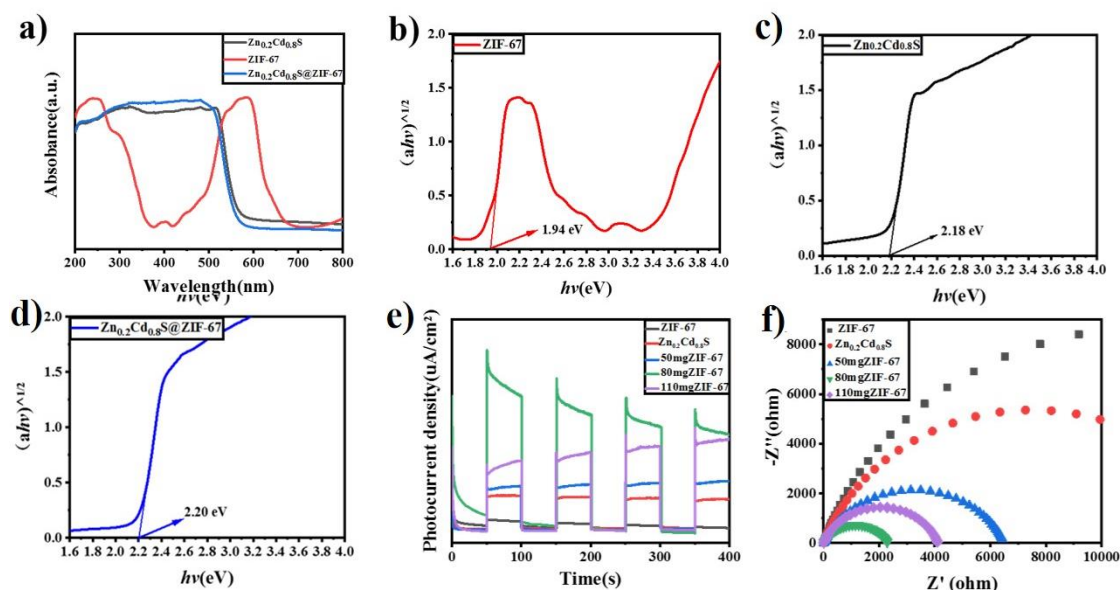


Figure 3. (a) UV-Vis DRS absorption spectra of $\text{Zn}_{0.2}\text{Cd}_{0.8}\text{S}$, ZIF-67 and $\text{Zn}_{0.2}\text{Cd}_{0.8}\text{S}@ZIF-67$; Band gap energy of (b) ZIF-67, (c) $\text{Zn}_{0.2}\text{Cd}_{0.8}\text{S}$ and (d) $\text{Zn}_{0.2}\text{Cd}_{0.8}\text{S}@ZIF-67$; (e) The instantaneous photocurrent diagram of $\text{Zn}_{0.2}\text{Cd}_{0.8}\text{S}@ZIF-67$; (f) The electrochemical impedance diagram of $\text{Zn}_{0.2}\text{Cd}_{0.8}\text{S}@ZIF-67$.

The photocatalytic activity of $\text{Zn}_{0.2}\text{Cd}_{0.8}\text{S}@ZIF-67$ was analyzed by an electrochemical experiment. In Figure 3e, ZIF-67, $\text{Zn}_{0.2}\text{Cd}_{0.8}\text{S}$, and $\text{Zn}_{0.2}\text{Cd}_{0.8}\text{S}@ZIF-67$ generate photocurrents before and after the light source is turned on. The photocurrent signal of $\text{Zn}_{0.2}\text{Cd}_{0.8}\text{S}@ZIF-67$ was more substantial than that of a single catalyst, and ZIF-67 was the weakest. When the additional amount of ZIF-67 is 80 mg, the fast photocurrent reaches the maximum. This indicates that the photocatalysis performance is the best. ZIF-67 has a large surface area, providing more photocatalytic active sites for $\text{Zn}_{0.2}\text{Cd}_{0.8}\text{S}$. It can better disperse $\text{Zn}_{0.2}\text{Cd}_{0.8}\text{S}$ and inhibit $\text{Zn}_{0.2}\text{Cd}_{0.8}\text{S}$ agglomeration. Thus, the light absorption ability of $\text{Zn}_{0.2}\text{Cd}_{0.8}\text{S}$ is improved. The existence of ZIF-67 is not only beneficial to the absorption of light by the catalyst, but also reduces the recombination of photoexcited electrons and holes. These effects shorten the transfer distance of charge carriers between the valence band and conduction band. The coordinated bandgap properties and close interaction between ZIF-67 and $\text{Zn}_{0.2}\text{Cd}_{0.8}\text{S}$ provide a new path for charge transfer.

The electrochemical impedance measurement is consistent with the instantaneous photocurrent measurement, as shown in Figure 3f. When the addition of ZIF-67 was 80 mg, the Nyquist diagram had the smallest arc radius, the slightest resistance, and the best photocatalytic performance. The results showed that ZIF-67 doped with $\text{Zn}_{0.2}\text{Cd}_{0.8}\text{S}$ could expose more catalytic active sites and promote the absorption of light energy.

The electron transfer behavior of ZIF-67, $\text{Zn}_{0.2}\text{Cd}_{0.8}\text{S}$, and $\text{Zn}_{0.2}\text{Cd}_{0.8}\text{S}@ZIF-67$ can be seen in Figure S2. Their separation abilities of light-generating carriers were characterized by fluorescence spectroscopy (PL). A high-intensity PL characteristic peak appears at 422 nm. The high electron-hole recombination ratio of ZIF-67 results in the intense luminescence emission of ZIF-67. Compared with ZIF-67, the fluorescence intensity of $\text{Zn}_{0.2}\text{Cd}_{0.8}\text{S}$ and $\text{Zn}_{0.2}\text{Cd}_{0.8}\text{S}@ZIF-67$ decreased significantly. This indicates that the carrier separation efficiency of these photocatalysts was higher than that of ZIF-67. Because of the doping of ZIF-67 into $\text{Zn}_{0.2}\text{Cd}_{0.8}\text{S}$, the crystalline size changed. The number of trapping sites of the luminescent electrons in $\text{Zn}_{0.2}\text{Cd}_{0.8}\text{S}@ZIF-67$ is reduced. This results in a lower luminous peak value for $\text{Zn}_{0.2}\text{Cd}_{0.8}\text{S}@ZIF-67$. Band gap characteristics and crystalline size changes of $\text{Zn}_{0.2}\text{Cd}_{0.8}\text{S}@ZIF-67$ increase the separating photogenerated electron and electron-hole pairs. This activity will further facilitate the photocatalyst degradation.

3.3. Photocatalyst Degradation of RhB

The photocatalytic degradation of RhB on $\text{Zn}_{0.2}\text{Cd}_{0.8}\text{S}@/\text{ZIF-67}$ was carried out at 10, 30, 50, and 70 mg, respectively (Figures S3 and S4). The C/C_0 of RhB with $\text{Zn}_{0.2}\text{Cd}_{0.8}\text{S}@/\text{ZIF-67}$ decreased with the illumination time (Figure 4a,b). In the dark adsorption equilibrium experiment, we can see that the degradation of RB increases from 10 to 50 mg. When the content of ZIF-67 was increased to 70 mg, C/C_0 decreased slightly. The best degradation performance was achieved under the addition of 50 and 70 mg of catalyst. C/C_0 was 98.40%. The large specific surface area of ZIF-67 can not only provide more active centers for the adsorption of reactants on the surface of the heterogeneous photocatalyst, but also shorten the transmission distance of carriers. A sufficient number of $\text{Zn}_{0.2}\text{Cd}_{0.8}\text{S}@/\text{ZIF-67}$ can reduce the occurrence of electron-hole pair recombination and accelerate the movement of charges between catalysts.

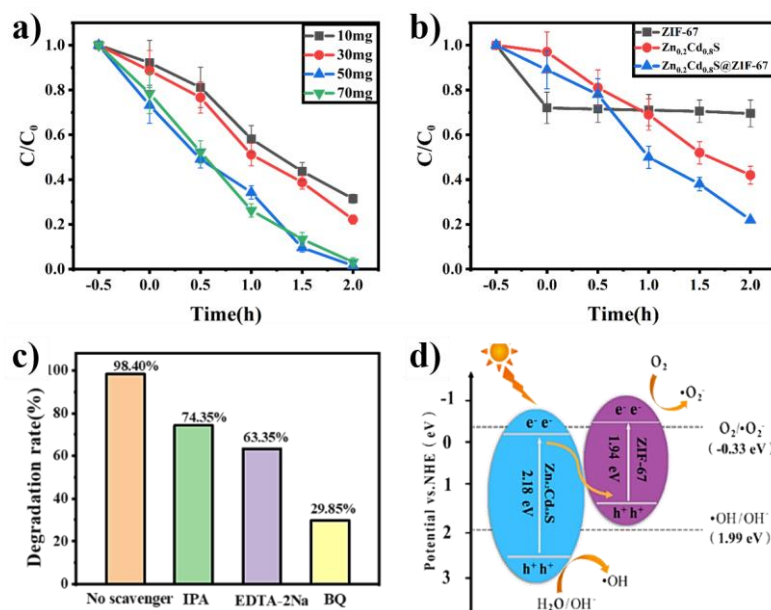


Figure 4. (a) C/C_0 of RhB varied with $\text{Zn}_{0.2}\text{Cd}_{0.8}\text{S}@/\text{ZIF-67}$; (b) C/C_0 of RhB with ZIF-67, $\text{Zn}_{0.2}\text{Cd}_{0.8}\text{S}$, and $\text{Zn}_{0.2}\text{Cd}_{0.8}\text{S}@/\text{ZIF-67}$; (c) Experiment of RhB capture by $\text{Zn}_{0.2}\text{Cd}_{0.8}\text{S}@/\text{ZIF-67}$ under Ultraviolet radiation. (d) Proposed Z-type photocatalytic system of $\text{Zn}_{0.2}\text{Cd}_{0.8}\text{S}@/\text{ZIF-67}$ under ultraviolet radiation.

The C/C_0 of ZIF-67, $\text{Zn}_{0.2}\text{Cd}_{0.8}\text{S}$, and $\text{Zn}_{0.2}\text{Cd}_{0.8}\text{S}@/\text{ZIF-67}$ are shown in Figure 4b. The mass of three catalysts were 30 mg. The concentration of RhB was selected to be 10 mg/L. In the dark environment, the C/C_0 of RhB by ZIF-67 is the highest, reaching 28.00%. The second is $\text{Zn}_{0.2}\text{Cd}_{0.8}\text{S}@/\text{ZIF-67}$, with C/C_0 of RhB increased to 11.35%. The lowest is C/C_0 of RhB by $\text{Zn}_{0.2}\text{Cd}_{0.8}\text{S}$, which is only 5.70%. Under visible light irradiation, ZIF-67 has little fluctuation in C/C_0 of RhB, about 30%. This indicates that light has little effect on its behavior. The degradation performance of RhB by $\text{Zn}_{0.2}\text{Cd}_{0.8}\text{S}$ and $\text{Zn}_{0.2}\text{Cd}_{0.8}\text{S}@/\text{ZIF-67}$ showed an upward trend with the increase of light time. The degradation performance was the largest when the illumination time was between 0.5 h and 1 h. During this time, C/C_0 reached 48.85% from 23.35%. Within 2 h, it reached 77.85%. On the one hand, this may be due to the morphological change of $\text{Zn}_{0.2}\text{Cd}_{0.8}\text{S}@/\text{ZIF-67}$ (as shown in SEM images in Figure 1c). The addition of ZIF-67 to $\text{Zn}_{0.2}\text{Cd}_{0.8}\text{S}$ results in smaller sized nanomaterials. On the other hand, the slightly larger crystal size of $\text{Zn}_{0.2}\text{Cd}_{0.8}\text{S}$ (shown in XRD results in Figure 1f) facilitated the electron transfer. The large surface area and mesoporous structure strengthens its adsorption and degradation ability. The electron movement space is wider, and the electron-hole pair becomes difficult to recombine, thereby improving the degradation performance of RhB.

As can be seen from Figure 4c, the final C/C_0 of RhB was 98.40% in RhB solution without a trapping agent, 74.35% in RhB solution with the trapping Agent IPA, and 63.35%

in RhB solution with EDTA-2Na. The addition of the capture agent BQ resulted in the worst degradation of RhB (29.85%), which was significantly less than that of no capture agent. The photocatalysis mechanism of $\text{Zn}_{0.2}\text{Cd}_{0.8}\text{S@ZIF-67}$ in photocatalytic degradation of RhB was further investigated (Figure 4d). EDTA-2Na is used as an h^+ trapping agent, BQ as $\cdot\text{O}_2^-$ trapping agent, and IPA as $\cdot\text{OH}$ trapping agent. It can be found that $\cdot\text{O}_2^-$ plays a significant role in the photocatalytic degradation of RhB. The following is h^+ , and finally, $\cdot\text{OH}$ scavenger.

The conduction band (CB) and valence band (VB) potentials of $\text{Zn}_{0.2}\text{Cd}_{0.8}\text{S}$ and ZIF-67 were estimated by electrochemical workstation, and Mott–Schottky diagrams were obtained (Figure S4). Both $\text{Zn}_{0.2}\text{Cd}_{0.8}\text{S}$ and ZIF-67 are n-type semiconductors [21,22]. The flat band potential of $\text{Zn}_{0.2}\text{Cd}_{0.8}\text{S}$ is estimated to be -0.27 eV [23], and ZIF-67 is -0.72 eV [24] by the Mott–Schottky method. For n-type semiconductors, the flat band potential is generally 0.1 eV more positive than the conduction potential [25]. Compared with the standard hydrogen electrode (0.24 eV, NHE), the conduction potential of $\text{Zn}_{0.2}\text{Cd}_{0.8}\text{S}$ is calculated to be $E_{\text{CB}} = -0.13$ eV, and the conduction potential of ZIF-67 is -0.58 eV (Figure S4). The valence band (E_{VB}) is derived from the formula $E_{\text{VB}} = E_{\text{G}} + E_{\text{CB}}$, the valence band of $\text{Zn}_{0.2}\text{Cd}_{0.8}\text{S}$ is 2.05 eV [26,27], and the valence band of ZIF-67 is 1.36 eV.

According to the derivation, the ZIF-67 valence band potential (1.36 eV) is lower than the standard OH potential (1.99 eV) [28], and the hole from the ZIF-67 valence band cannot oxidize the water molecule to $\cdot\text{OH}$. This suggests that the holes in the ZIF-67 valence band do not have enough energy to oxidize OH^- or H_2O to $\cdot\text{OH}$. The electrons in the $\text{Zn}_{0.2}\text{Cd}_{0.8}\text{S}$ conduction band do not have enough energy to reduce O_2 to $\cdot\text{O}_2^-$ because the potential of the $\text{Zn}_{0.2}\text{Cd}_{0.8}\text{S}$ conduction band is higher than $E_{\theta}(\text{O}_2/\cdot\text{O}_2^-)$ (-0.33 eV, NHE). The h^+ , $\cdot\text{O}_2^-$, and $\cdot\text{OH}$ are the main active substances in the degradation of RhB [29,30]. The type II heterostructure system [31] obviously cannot explain the photoelectron and hole transfer process of $\text{Zn}_{0.2}\text{Cd}_{0.8}\text{S@ZIF-67}$ [32,33].

Based on the above derivation results, we propose a Z-type photocatalytic mechanism. Under visible light irradiation, the $\text{Zn}_{0.2}\text{Cd}_{0.8}\text{S}$ and ZIF-67 conduction bands are excited to generate electrons, and holes are generated on the valence band. CB (-0.58 eV) of ZIF-67 is lower than $E_{\theta}(\text{O}_2/\cdot\text{O}_2^-)$ (-0.33 eV). Therefore, photogenerated electrons reduce O_2 to form the active substance ($\cdot\text{O}_2^-$). The VB (2.05 eV) potential of $\text{Zn}_{0.2}\text{Cd}_{0.8}\text{S}$ is higher than that of $E_{\theta}(\cdot\text{OH}/\text{H}_2\text{O})$ (1.99 eV), which means that photogenerated holes will generate active substances and ($\cdot\text{OH}$) from OH^- . At the same time, some electrons in the CB of $\text{Zn}_{0.2}\text{Cd}_{0.8}\text{S}$ will quickly bind to the holes in the VB of ZIF-67. This means that the electrons in the ZIF-67 conduction band have enough energy to reduce O_2 to O_2^- . The holes in the $\text{Zn}_{0.2}\text{Cd}_{0.8}\text{S}$ valence band have enough energy to oxidize H_2O to OH . Ultimately, $\cdot\text{OH}$ and $\cdot\text{O}_2^-$ as active species may be involved in photooxidation and degradation of RhB. The heterojunction between $\text{Zn}_{0.2}\text{Cd}_{0.8}\text{S}$ and ZIF-67 can significantly enhance the separation of e^-/h^+ and improve charge transfer at the interface. The formation of this heterojunction can not only accelerate the separation and transfer rate of photogenerated charges, but also maintain a strong redox ability and effectively degrade the dye RhB.

3.4. DA Sensor and Mechanism Exploration

$\text{Zn}_{0.2}\text{Cd}_{0.8}\text{S@ZIF-67}$ was dissolved in a mixture of ethanol and Nafion and sonicated. Suspension droplets were applied to a clean screen-printed electrode (SPCE) and dried. $\text{Zn}_{0.2}\text{Cd}_{0.8}\text{S@ZIF-67}/\text{SPCE}$ was formed and used to measure the photocurrent of DA hydrochloride under illumination. In Figure 5a, the current changes at different DA concentrations under light irradiation are presented. At the constant DA concentration, with the light on at 100 s, the current increased to a plateau and maintained constance. When the light turned off after 50 s, the detection current decreased to the previous base line. In Figure 5b, the DA with the concentration of 30 M to 2 mM can be detected. It was found that polydopamine produced by oxidation of DA could effectively enhance the photocurrent. However, it is notable that the detection current is not high enough for a concentration-dependent analysis. This may be due to the morphology of $\text{Zn}_{0.2}\text{Cd}_{0.8}\text{S@ZIF-67}$.

The 0D $\text{Zn}_{0.2}\text{Cd}_{0.8}\text{S}$ particles combined with 3D ZIF-67 shells inhibit the charge transfer within the system. Additional 1D and 2D nanomaterials might be a solution for bridging the charge transfer between 0D and 3D nanomaterials.

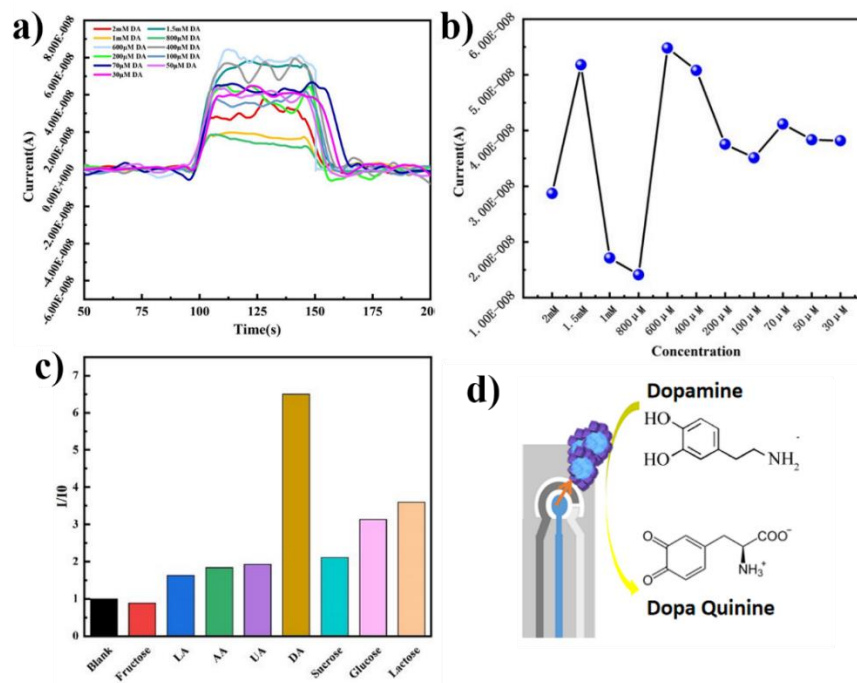


Figure 5. (a) DA sensing photocurrent response; (b) the sensitivity and (c) selectivity of the $\text{Zn}_{0.2}\text{Cd}_{0.8}\text{S@ZIF-67}$ to DA; (d) photocatalytic mechanism of $\text{Zn}_{0.2}\text{Cd}_{0.8}\text{S@ZIF-67}$ as DA sensor.

The selectivity of $\text{Zn}_{0.2}\text{Cd}_{0.8}\text{S@ZIF-67}$ toward DA was evaluated by using a CHI760E platform. In human blood plasma, DA co-exists with many kinds of biomolecules, such as AA, UA, and glucose. It is essential to confirm the ability of the catalyst for the selection detection of DA. Herein, we selected fructose, LA, AA, UA, sucrose, glucose, and lactose as the interfering molecules toward DA. As shown in Figure 5c, the amperometric current change is evident with the addition of DA, while there is relatively little change with the addition of the same amount interfering molecules. Taken together, we can come to the conclusion that $\text{Zn}_{0.2}\text{Cd}_{0.8}\text{S@ZIF-67}$ is a promising platform for DA detection.

Although the detection sensitivity is not high enough, $\text{Zn}_{0.2}\text{Cd}_{0.8}\text{S@ZIF-67}$ displayed outstanding selectivity toward DA. Photocurrent promotion toward DA may be attributed to the interaction between photogenerated electrons and electron receptors (Figure 5d). On the one hand, through radical capture experiments, superoxide radicals ($\cdot\text{O}_2^-$) played a major role in the DA sensing. On the other hand, the structure of ZIF-67 can provide more photocatalytic activity check points for $\text{Zn}_{0.2}\text{Cd}_{0.8}\text{S}$ and enhance the sensing efficiency of DA. In addition, the heterojunction between $\text{Zn}_{0.2}\text{Cd}_{0.8}\text{S}$ and ZIF-67 can significantly enhance the separation of e^-/h^+ and improve charge transfer at the PEC interface. Therefore, in the presence of DA hydrochloride, the two free phenolic hydroxyl groups can act as an effective electron donor for the photoexcited $\text{Zn}_{0.2}\text{Cd}_{0.8}\text{S@ZIF-67}$ and promote charge transfer from $\text{Zn}_{0.2}\text{Cd}_{0.8}\text{S}$ to ZIF-67, thus resulting in the anodic photocurrent and DA sensing. The results provide a possibility to construct the PEC sensor platform for DA detection.

4. Conclusions

In this study, $\text{Zn}_{0.2}\text{Cd}_{0.8}\text{S@ZIF-67}$ was prepared via a hydrothermal method. The photocurrent intensity of $\text{Zn}_{0.2}\text{Cd}_{0.8}\text{S@ZIF-67}$ was the highest, and the electrode resistance was the lowest, when the addition of ZIF-67 reached 80 mg. Meanwhile, $\text{Zn}_{0.2}\text{Cd}_{0.8}\text{S@ZIF-67}$ shows lower fluorescence intensity in PL spectra, indicating fewer electron-hole recombination. When the dosage of $\text{Zn}_{0.2}\text{Cd}_{0.8}\text{S@ZIF-67}$ reached 50 mg, the degradation percentage

reached the maximum of 98.40%. In addition, a superoxide radical ($\cdot\text{O}_2^-$) plays a major role in the degradation of RhB, confirmed by free radical capture experiments. Finally, the DA sensor modified with $\text{Zn}_{0.2}\text{Cd}_{0.8}\text{S}/\text{ZIF-67}$ exhibits excellent selectivity and high response within the DA concentration of 30 nM to 2 mM. This study provides strategies for developing cost-efficient, highly selective DA detection methods.

Supplementary Materials: The following supporting information can be downloaded at: <https://www.mdpi.com/article/10.3390/ma15217683/s1>, Figure S1: High-resolution XPS spectrum; Figure S2: Steady-state fluorescence spectra; Figure S3: UV-Vis spectrogram; Figure S4: The pseudo-first-order kinetics of RhB; Figure S5: Mott-Schottky plots; Table S1: XRD peaks analysis.

Author Contributions: Writing—original draft preparation, data curation, supervision, Z.W.; supervision, writing—review and editing, B.W.; formal analysis and data curation, J.Z.; data curation, X.Z. (Xin Zhao); formal analysis, writing—review and editing, supervision, X.Z. (Xiaoyuan Zhang); supervision, writing—review and editing, Z.S. All authors have read and agreed to the published version of the manuscript.

Funding: This research was funded by the Key Laboratory of Processing and Quality Evaluation Technology of Green Plastics of China National Light Industry Council, the Beijing Technology and Business University (PQETGP2022005), and the Beijing Science and Technology Plan Project (Z211100004321003, Z211100004321004). This research received no external funding from the Fundamental Research Funds for the Central Universities (ZY2103).

Institutional Review Board Statement: Not applicable.

Informed Consent Statement: Not applicable.

Conflicts of Interest: The authors declare no conflict of interest.

References

1. Klein, M.O.; Battagello, D.S.; Cardoso, A.R.; Hauser, D.N.; Bittencourt, J.C.; Correa, R.G. Dopamine: Functions, Signaling, and Association with Neurological Diseases. *Cell. Mol. Neurobiol.* **2019**, *39*, 31–59. [[CrossRef](#)] [[PubMed](#)]
2. Kim, S.G.; Lee, J.S. Ruthenium Nanoparticle-Immobilized Porous Carbon Nanofibers for Nonenzymatic Dopamine Sensing. *ACS Appl. Nano Mater.* **2021**, *4*, 13683–13691. [[CrossRef](#)]
3. Harley, C.C.; Rooney, A.D.; Breslin, C.B. The selective detection of dopamine at a polypyrrole film doped with sulfonated β -cyclodextrins. *Sens. Actuators B Chem.* **2010**, *150*, 498–504. [[CrossRef](#)]
4. Dashtian, K.; Hajati, S.; Ghaedi, M. Ti-Based Solid-State Imprinted- $\text{Cu}_2\text{O}/\text{CuInSe}_2$ Heterojunction Photoelectrochemical platform for Highly Selective Dopamine Monitoring. *Sens. Actuators B Chem.* **2021**, *326*, 128824. [[CrossRef](#)]
5. Chen, Y.; Li, J.; Zhai, B.; Liang, Y. Enhanced photocatalytic degradation of RhB by two-dimensional composite photocatalyst. *Colloids Surf. A Physicochem. Eng. Asp.* **2019**, *568*, 429–435. [[CrossRef](#)]
6. Liu, W.; Yang, Y.; Yang, X.; Peng, Y.-L.; Cheng, P.; Zhang, Z.; Chen, Y. Template-Directed Fabrication of Highly Efficient Metal-Organic Framework Photocatalysts. *ACS Appl. Mater. Interfaces* **2021**, *13*, 58619–58629. [[CrossRef](#)]
7. Wang, D.; Zhu, R.; Lou, J.; Yuan, J.; Xu, J.; Fan, X. Novel marigold-like CuO/Cu -based MOFs composite photocatalyst for high-performance removal of alkylphenol ethoxylate under visible light. *J. Environ. Chem. Eng.* **2021**, *9*, 106434. [[CrossRef](#)]
8. Zou, X.-N.; Zhang, D.; Luan, T.-X.; Li, Q.; Li, L.; Li, P.-Z.; Zhao, Y. Incorporating Photochromic Triphenylamine into a Zirconium-Organic Framework for Highly Effective Photocatalytic Aerobic Oxidation of Sulfides. *ACS Appl. Mater. Interfaces* **2021**, *13*, 20137–20144. [[CrossRef](#)]
9. La Ngoc Tran, N.; Phan, B.T.; Ta, H.K.T.; Chi, T.T.K.; Hien, B.T.T.; Phuong, N.T.T.; Nguyen, C.C.; Doan, T.L.H.; Tran, N.H.T. Gold nanoparticles are capped under the IRMOF-3 platform for in-situ surface-enhanced Raman scattering technique and optic fiber sensor. *Sens. Actuators A Phys.* **2022**, *347*, 113932. [[CrossRef](#)]
10. He, H.; Li, R.; Yang, Z.; Chai, L.; Jin, L.; Alhassan, S.I.; Ren, L.; Wang, H.; Huang, L. Preparation of MOFs and MOFs derived materials and their catalytic application in air pollution: A review. *Catal. Today* **2021**, *375*, 10–29. [[CrossRef](#)]
11. Li-Li, Z.; Liu, M.; Ke-An, W.; Hai-Bin, Z. Assembling $\text{Ag}/\text{UiO-66-NH}_2$ Composites for Photocatalytic Dye Degradation. *J. Inorg. Organomet. Polym. Mater.* **2022**, *32*, 1896–1901. [[CrossRef](#)]
12. Dong, Y.-J.; Jiang, Y.; Liao, J.-F.; Chen, H.-Y.; Kuang, D.-B.; Su, C.-Y. Construction of a ternary $\text{WO}_3/\text{CsPbBr}_3/\text{ZIF-67}$ heterostructure for enhanced photocatalytic carbon dioxide reduction. *Sci. China Mater.* **2022**, *65*, 1550–1559. [[CrossRef](#)]
13. Kumar, O.P.; Ahmad, M.; Nazir, M.A.; Anum, A.; Jamshaid, M.; Shah, S.S.A.; Rehman, A. Strategic combination of metal-organic frameworks and C_3N_4 for expeditious photocatalytic degradation of dye pollutants. *Environ. Sci. Pollut. Res.* **2022**, *29*, 35300–35313. [[CrossRef](#)] [[PubMed](#)]

14. Rafiq, A.; Imran, M.; Aqeel, M.; Naz, M.; Ikram, M.; Ali, S. Study of Transition Metal Ion Doped CdS Nanoparticles for Removal of Dye from Textile Wastewater. *J. Inorg. Organomet. Polym. Mater.* **2020**, *30*, 1915–1923. [[CrossRef](#)]
15. Junaid, M.; Imran, M.; Ikram, M.; Naz, M.; Aqeel, M.; Afzal, H.; Majeed, H.; Ali, S. The study of Fe-doped CdS nanoparticle-assisted photocatalytic degradation of organic dye in wastewater. *Appl. Nanosci.* **2019**, *9*, 1593–1602. [[CrossRef](#)]
16. Zhang, X.; Peng, J.; Song, Y.; Chen, Y.; Lu, F.; Gao, W. Porous hollow carbon nanobubbles@ZnCdS multi-shelled dodecahedral cages with enhanced visible-light harvesting for ultrasensitive photoelectrochemical biosensors. *Biosens. Bioelectron.* **2019**, *133*, 125–132. [[CrossRef](#)]
17. Jin, Z.; Liu, Y.; Hao, X. Self-assembly of zinc cadmium sulfide nanorods into nanoflowers with enhanced photocatalytic hydrogen production activity. *J. Colloid Interface Sci.* **2020**, *567*, 357–368. [[CrossRef](#)]
18. Liu, K.; Peng, L.; Zhen, P.; Chen, L.; Song, S.; Garcia, H.; Sun, C. ZnCdS Dotted with Highly Dispersed Pt Supported on SiO₂ Nanospheres Promoting Photocatalytic Hydrogen Evolution. *J. Phys. Chem. C* **2021**, *125*, 14656–14665. [[CrossRef](#)]
19. Chen, M.; Huang, X.; Chen, C.; Hou, W.; Xu, Y. M-Dependent activity of MCo₂O₄ spinels for water splitting and H₂ production on Zn_{0.5}Cd_{0.5}S under visible light. *Appl. Catal. B-Environ.* **2021**, *298*, 120469. [[CrossRef](#)]
20. Zhang, X.; Peng, J.; Ding, Y.; Zheng, D.; Lin, Y.; Chen, Y.; Gao, W. Rationally designed hierarchical hollow ZnCdS@MoS₂ heterostructured cages with efficient separation of photogenerated carriers for photoelectrochemical aptasensing of lincomycin. *Sens. Actuators B-Chem.* **2020**, *306*, 127552. [[CrossRef](#)]
21. Wang, L.; Wang, X.-A.; Chen, R.; Wu, C.-Y.; Yu, Y.-Q.; Xu, J.; Hu, J.-G.; Luo, L.-B. Gallium doped n-type Zn_xCd_{1-x}S nanoribbons: Synthesis and photoconductivity properties. *J. Appl. Phys.* **2014**, *115*, 063108. [[CrossRef](#)]
22. Yan, X.; Jin, Z.; Zhang, Y.; Zhang, Y.; Yuan, H. Sustainable and efficient hydrogen evolution over a noble metal-free WP double modified Zn_xCd_{1-x}S photocatalyst driven by visible-light. *Dalton Trans.* **2019**, *48*, 11122–11135. [[CrossRef](#)] [[PubMed](#)]
23. Sun, Y.; Xu, C.; Ma, H.; Li, G.; Chen, L.; Sun, Y.; Chen, Z.; Fang, P.; Fu, Q.; Pan, C. Synthesis of flower-like twin crystal ternary Ni/NiS/Zn_{0.2}Cd_{0.8}S catalyst for highly efficient hydrogen production. *Chem. Eng. J.* **2021**, *406*, 126878. [[CrossRef](#)]
24. Wang, G.; Li, Y.; Xu, L.; Jin, Z.; Wang, Y. Facile synthesis of difunctional NiV LDH@ZIF-67 p-n junction: Serve as prominent photocatalyst for hydrogen evolution and supercapacitor electrode as well. *Renew. Energy* **2020**, *162*, 535–549. [[CrossRef](#)]
25. Zhou, L.; Dai, S.; Xu, S.; She, Y.; Li, Y.; Leveneur, S.; Qin, Y. Piezoelectric effect synergistically enhances the performance of Ti₃₂-oxocluster/BaTiO₃/CuS p-n heterojunction photocatalytic degradation of pollutants. *Appl. Catal. B Environ.* **2021**, *291*, 120019. [[CrossRef](#)]
26. Yin, L.; Zhang, F.; Feng, L.; Huang, J.; Kong, X.; Zhang, H.; Li, H.; Wang, X. Constructing 3D hierarchical Zn_{0.2}Cd_{0.8}S microspheres for the improved visible-light-driven photocatalytic performance. *Int. J. Hydrogen Energy* **2019**, *44*, 23868–23879. [[CrossRef](#)]
27. Guo, H.; Ding, J.; Wan, S.; Wang, Y.; Zhong, Q. Highly efficient CH₃OH production over Zn_{0.2}Cd_{0.8}S decorated g-C₃N₄ heterostructures for the photoreduction of CO₂. *Appl. Surf. Sci.* **2020**, *528*, 146943. [[CrossRef](#)]
28. Wang, Q.; Wang, P.; Xu, P.; Li, Y.; Duan, J.; Zhang, G.; Hu, L.; Wang, X.; Zhang, W. Visible-light-driven photo-Fenton reactions using Zn_{1-1.5x}Fe_xS/g-C₃N₄ photocatalyst: Degradation kinetics and mechanisms analysis. *Appl. Catal. B-Environ.* **2020**, *266*, 118653. [[CrossRef](#)]
29. Yu, H.; Xu, S.; Zhang, S.; Wang, S.; He, Z. In-situ construction of core-shell structured TiB₂-TiO₂@g-C₃N₄ for efficient photocatalytic degradation. *Appl. Surf. Sci.* **2022**, *579*, 152201. [[CrossRef](#)]
30. Feng, J.; Zhang, D.; Zhou, H.; Pi, M.; Wang, X.; Chen, S. Coupling P Nanostructures with P-Doped g-C₃N₄ As Efficient Visible Light Photocatalysts for H₂ Evolution and RhB Degradation. *ACS Sustain. Chem. Eng.* **2018**, *6*, 6342–6349. [[CrossRef](#)]
31. Wang, Y.; Lu, N.; Luo, M.; Fan, L.; Zhao, K.; Qu, J.; Guan, J.; Yuan, X. Enhancement mechanism of fiddlehead-shaped TiO₂-BiVO₄ type II heterojunction in SPEC towards RhB degradation and detoxification. *Appl. Surf. Sci.* **2019**, *463*, 234–243. [[CrossRef](#)]
32. Cui, Z.; Wu, H.; Bai, K.; Chen, X.; Li, E.; Shen, Y.; Wang, M. Fabrication of a g-C₃N₄/MoS₂ photocatalyst for enhanced RhB degradation. *Phys. E Low-Dimens. Syst. Nanostruct.* **2022**, *144*, 115361. [[CrossRef](#)]
33. Frindy, S.; Sillanpää, M. Synthesis and application of novel α-Fe₂O₃/graphene for visible-light enhanced photocatalytic degradation of RhB. *Mater. Des.* **2020**, *188*, 108461. [[CrossRef](#)]